Chemical Engineering Journal 524 (2025) 169248

Contents lists available at ScienceDirect

Chemical Engineering Journal

journal homepage: www.elsevier.com/locate/cej

Semi-automated computational investigation of the oxidative degradation mechanisms of bisphenol A in Fenton-type processes

Pablo A. Chacón-Morales [a], Antonio Fernández-Ramos [a,b], Jorge González-Rodríguez [c], María Teresa Moreira [c], Emilio Martínez-Núñez [a], David Ferro-Costas [a,*]

[a] Departamento de Química Física, Universidade de Santiago de Compostela, 15782, Santiago de Compostela, Spain
[b] Centro Singular de Investigación en Química Biolóxica e Materiais Moleculares (CIQUS), Universidade de Santiago de Compostela, 15782, Santiago de Compostela, Spain
[c] CRETUS, Department of Chemical Engineering, School of Engineering, University of Santiago de Compostela, 15782, Santiago de Compostela, Spain

ARTICLE INFO

Keywords:
BPA oxidative degradation
Autonomous reaction mechanism discovery
Kinetic modeling
AutoMeKin
Pilgrim

ABSTRACT

Bisphenol A (BPA) is a widespread industrial contaminant and endocrine disruptor whose efficient removal remains challenging because multiple, competing radical channels operate under Fenton-type advanced oxidation conditions. Here, we present a semi-automated first-principles approach to elucidate this process, comprising: (i) exhaustive discovery of unimolecular radical transformations with *AutoMeKin*; (ii) targeted manual construction of initial •OH addition and hydrogen-abstraction transition states; (iii) DFT refinement at ωB97XD/def2-TZVPP with SMD solvation model; (iv) selective microsolvation (up to two water molecules) for high potential energy barriers; (v) transition state theory rate constants evaluation for all elementary steps, and unified statistical treatment of dual bottlenecks for bimolecular •OH reactions; and (vi) Kinetic Monte Carlo (KMC) simulations with *Pilgrim* to obtain product distributions.

The reaction network maps all feasible early •OH additions (*ipso/ortho/meta/para*), phenolic O—H abstraction, multistep hydroxylations, attempted dehydration steps, epoxidation, ring opening, and C—C scission leading to hydroxylated, quinonoid, lactone, and cleavage products. Selective microsolvation lowers critical rearrangement barriers, converting otherwise rate-determining steps into kinetically viable channels. KMC analysis identifies a characteristic ≈2:1 [•OH]:[BPA] threshold. Below it, early hydroxylated and ketone intermediates persist (e.g., catecholic and cyclohexadienone forms), whereas above it they are rapidly converted into trihydroxylated derivatives, ring-cleavage fragments, and quinone products.

A reduced mechanism derived from sensitivity analysis reproduces the kinetics of the full network while retaining only essential OH-addition and phenolic H-abstraction steps. This integrated workflow thus provides mechanistic insight and a predictive, computationally efficient kinetic model readily transferable to other organic contaminants in advanced oxidation processes.

1. Introduction

Among the wide variety of environmental pollutants, bisphenol A (BPA) and its derivatives have garnered considerable attention due to their widespread presence in wastewater from various industrial processes [1,2]. Their high water solubility and persistence against degradation lead to the accumulation of BPA derivatives in aquatic environments, posing serious concerns due to their detrimental effects on aquatic ecosystems [1–4] and their known carcinogenic and genotoxic properties [5,6]. These concerns have motivated extensive experimental and theoretical efforts to better understand the degradation mechanisms of these compounds.

On the experimental side, numerous studies have explored the efficient removal of BPA using a variety of techniques, including advanced oxidation processes (AOPs), electrochemical degradation, biological treatments, membrane filtration, UV irradiation, and more [7–13]. Among AOPs, the Fenton reaction [14] is one of the most widely studied and applied methods for the degradation of organic contaminants in water. It involves the catalytic decomposition of hydrogen peroxide by ferrous ions ($Fe^{2+} + H_2O_2 \rightarrow Fe^{3+} + {}^{\bullet}OH + OH^-$; $Fe^{3+} + H_2O_2 \rightarrow Fe^{2+} +$

* Corresponding author.
E-mail address: david.ferro@usc.es (D. Ferro-Costas).

https://doi.org/10.1016/j.cej.2025.169248
Received 11 July 2025; Received in revised form 25 September 2025; Accepted 2 October 2025
Available online 6 October 2025

$^{\bullet}OOH + H^{+}$), leading to the in situ generation of hydroxyl radicals ($^{\bullet}OH$). These species are highly reactive and non-selective, capable of initiating multiple degradation pathways of aromatic pollutants such as BPA. The Fenton system thus provides a well-established reference framework for investigating radical-driven degradation mechanisms under aqueous conditions.

On the computational side, there has been a notable rise in the use of modeling approaches to study chemical reactions involved in pollutant transformation [1,15,16]. Central to these computational methods are density functional theory (DFT) calculations, which can be employed to determine the binding energies of chemical species, assess the feasibility of reaction pathways, and evaluate the physicochemical properties of molecules within the context of environmental chemistry [17–19]. The application of DFT simulations deepens our understanding of reaction systems, optimizing their efficiency while reducing the consumption of chemical reagents, waste generation, and the substantial workload typically associated with experimental work [20]. In fact, most previous computational studies on BPA degradation predominantly rely on DFT calculations and/or Fukui function analyses to predict the early stages of the degradation process [21–29]. While these previous efforts are commendable, the complexity of the system necessitates a bias-free approach to ensure that no potential reaction pathways are overlooked.

As part of our research efforts to deepen the understanding of reaction mechanisms and kinetics, we have developed two open-source programs in recent years: *AutoMeKin* [30], designed for the autonomous discovery of reaction mechanisms, and *Pilgrim* [31], which calculates thermal rate constants for chemical reactions and simulates complex reaction networks by Kinetic Monte Carlo [32]. *AutoMeKin* has been successfully applied to study a wide range of problems in astrochemistry [33–36], carbon-based materials [37], homogeneous catalysis [38], radiation damage of biological systems [39], simulation of mass spectrometry experiments [40,41], combustion chemistry [42,43], and atmospheric chemistry [44]. A complete list of recent works utilizing *AutoMeKin* can be found in [45].

Pilgrim, on the other hand, has been effectively used in systems spanning from low-temperature processes, such as the formation of methanol dimers [46] and the tautomerization of urea derivatives at 10 K [47], to high-temperature combustion reactions involving biofuels [42,48]. Additionally, *Pilgrim* has proven valuable in calculating kinetic isotopic effects in aqueous solution [49], in studies of biological relevance, such as the isomerization of vitamin D [50], as well as in the investigation of metal-organic framework-catalyzed reactions [51]. These diverse applications highlight *Pilgrim*'s versatility and reliability in determining thermal rate constants across different chemical environments.

AutoMeKin and *Pilgrim* have been also previously used in combination [33,42]. The primary advantage of our computational methods over more conventional approaches is their ability to eliminate human bias in predicting reaction mechanisms, while also providing a reliable protocol for simulating chemical kinetics under a wide range of conditions. In this study, we will explore the initial steps of BPA degradation in a Fenton-type environment, integrating our computational methods with DFT calculations. Furthermore, the results from our kinetic modeling will provide detailed insights into the degradation mechanisms and corresponding timescales.

2. Materials and methods

The experimental and computational protocols employed in this work are detailed in the following three sections. The first section presents the experimental determination of the rate of formation of the OH radical in the Fenton reaction. The second one describes the generation of the reaction mechanism, while the third outlines the formalism used for the kinetic modeling conducted in this study. Notice that all the data generated using our computational protocol is publicly available in a Zenodo repository [52].

2.1. Experimental determination of OH radical formation

The determination of the rate of formation of the OH radicals in the Fenton reaction was carried out using methanol as the reacting agent, since methanol acts as a scavenger of these radicals with high kinetic rate and selectivity [53,54]. To avoid the influence of methanol concentration, an excess of this reagent was used, with an initial concentration of 18.88 mM, ensuring that its decrease remained below 5 %. This prevented the occurrence of side reactions and guaranteed that the main reaction predominated [55]. Measurements were taken during the first 30 min, and methanol concentration was determined by gas chromatography.

The quantification of OH formation through methanol consumption was performed using gas chromatography equipped with a flame ionization detector (GC-6850-FID) and a DB-WAX column (30 m × 0.250 mm × 0.25 μm), both purchased from Agilent Technologies Inc. (CA, USA). Nitrogen was used as the carrier gas at a flow rate of 1 mL min^{-1} (split ratio 5:1, pressure 12–18 psi), with an injection volume of 1 μL. The column temperature program consisted of an initial hold at 70 °C for 3 min, followed by a ramp of 60 °C min^{-1} up to 220 °C, maintained for 5 min. The injector and detector temperatures were set at 250 °C and 300 °C, respectively. The equipment was calibrated using methanol standard solutions in the range of 3–20 mM.

All experiments were performed in triplicate under the optimum Fenton conditions, namely with 131 mg/L of Fe_3O_4@PAA/SBA15 nanoparticles [56] and 223 mg/L of hydrogen peroxide. The resulting data were fitted to zero-order reaction kinetics, and the OH radical generation rate was quantified as 17 ± 2 μM·min^{-1}, as shown in Fig. 1.

2.2. Reaction mechanism

The computational study of BPA degradation pathways under Fenton-type conditions was conducted in a semi-automated manner. While the (bimolecular) OH addition and H-abstraction steps were studied manually, the unimolecular evolutions of the intermediate radical species were elucidated using an automated method for reactive potential energy surface (PES) exploration. The only exceptions to this automation were the unimolecular pathways in which water molecules were included explicitly.

Bimolecular elementary steps are studied using the traditional approach of manually constructing initial guesses for transition state (TS). To simplify the problem, the bimolecular OH-addition and H-

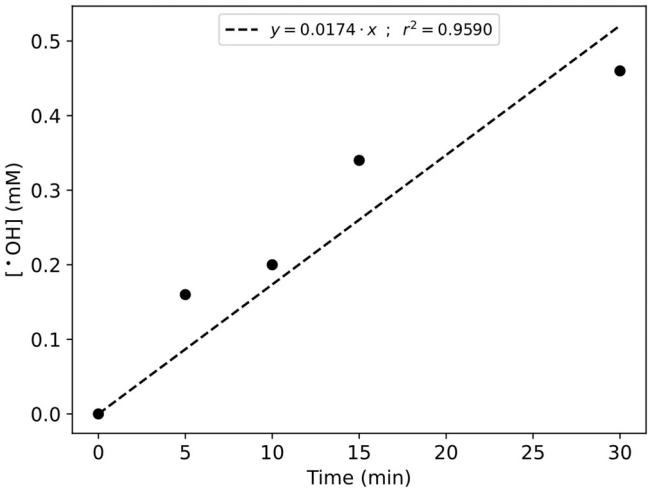

Fig. 1. Time evolution of the hydroxyl radical concentration from 0 to 30 min. Symbols denote experimental data; the dashed line is a linear fit constrained to pass through the origin. The slop represents the apparent OH radical generation rate.

abstraction steps treat certain carbon atoms in BPA as equivalent, with the corresponding rate coefficients incorporating reaction path degeneracies ($\sigma > 1$) [57]. This process involves optimizing the TSs, calculating their vibrational frequencies, and following the minimum energy pathways (MEPs) [58] that connect reactants and products. All calculations are performed using Gaussian16 [59] at the ωB97XD/def2-TZVPP DFT level of theory. This model chemistry is known for its strong performance in predicting barrier heights [60]. Since our goal is to simulate the degradation of BPA in water, the energies of the obtained stationary points were corrected using the solvation model density (SMD) [61] implemented in Gaussian16.

On the other hand, the unimolecular evolution of the identified intermediate species was investigated using our own autonomous mechanism generator algorithm [30,62,63]. The method has been implemented in the open-source package *AutoMeKin* [64] and utilizes reactive molecular dynamics (MD) simulations to search for stationary points.

Briefly, *AutoMeKin* leverages reactive MD simulations to explore the PES of a system. A post-processing analysis of the 1-fs resolution MD snapshots allows for the identification of suitable TS candidates. After partially relaxing the initially highly distorted structure, a transition state is fully optimized using MOPAC's built-in eigen-vector following algorithm [65,66]. Once a TS is optimized, the workflow proceeds with a MEP calculation [58] to identify the corresponding reactant and product for the elementary step. The outcome is the so-called reaction network (RXNet), which includes the set of reactants, products, and reactions. The analysis of the RXNets is significantly enhanced by the use of *amk_tools* [67,68]. *AutoMeKin* employs a hierarchy of electronic structure levels of theory:

1. Level 1. The semi-empirical method PM7 [69] is used for exploratory MD simulations.
2. Level 2. The cost-effective ab initio method, HF/3-21G, is utilized to filter out spurious structures obtained at Level1. Fig. 2 shows an example of the RXNet obtained using Level2 for the unimolecular reactions of the radical species R01 identified in this work (see Section 3), following processing with *amk_tools*.
3. Level 3. The same level of theory employed to map the bimolecular reactions, ωB97XD/def2-TZVPP optimizations with SMD single-point corrections, was also employed to refine the energies, vibrational frequencies, and geometries of the stationary points corresponding to pathways with Level2-calculated energy barriers lower than 40 kcal·mol^{-1}. The rationale for establishing a maximum threshold for Gibbs activation energies is that unimolecular reactions with high barriers cannot compete with the corresponding bimolecular reactions involving hydroxyl radicals and can, therefore, be safely ruled out. Nevertheless, we decided to apply a relatively high threshold for the barrier heights since Hartree-Fock is known to significantly overestimate them [70].

For Level 1, we used MOPAC, which is integrated into *AutoMeKin*, while for Level 2 and Level 3, we utilized the external Gaussian16 package [59]. At the Level 3 stage, we also examined the effect of microsolvation by including up to two explicit water molecules in some selected unimolecular pathways, while applying the same SMD solvation corrections. This allowed us to account for specific solvent interactions where relevant (see Section 3).

Finally, it should be noted that this workflow can be considered semi-automated unimolecular reactivity was fully explored automatically with *AutoMeKin*, but manual construction was required for selected bimolecular steps and solvent-assisted transformations, for which no general automated protocol is currently available.

2.3. Kinetic modeling

The reaction mechanisms obtained as described above are then used as input for *Pilgrim* [31] to model the system's kinetics under experimental conditions. *Pilgrim* is an open-source package designed to accurately calculate thermal rate coefficients and solve systems of kinetic differential equations. The coupled kinetic equations, also known as the chemical master equation (CME), are solved using the Kinetic Monte Carlo (KMC) method [32]. The CME can be expressed as follows.

$$\frac{d\mathbf{p}}{dt} = \mathbf{\Omega} \bullet \mathbf{p} \tag{1}$$

where t denotes time, $\mathbf{p}$ is the vector representing the population of each chemical species as a function of time, and $\mathbf{\Omega}$ is the transition matrix containing the rate coefficients for all elementary steps.

Our kinetic simulations are based on the following initial conditions: [BPA] = 1.31 μM, [H_2O] = 55.5 M, with the concentration of hydroxyl

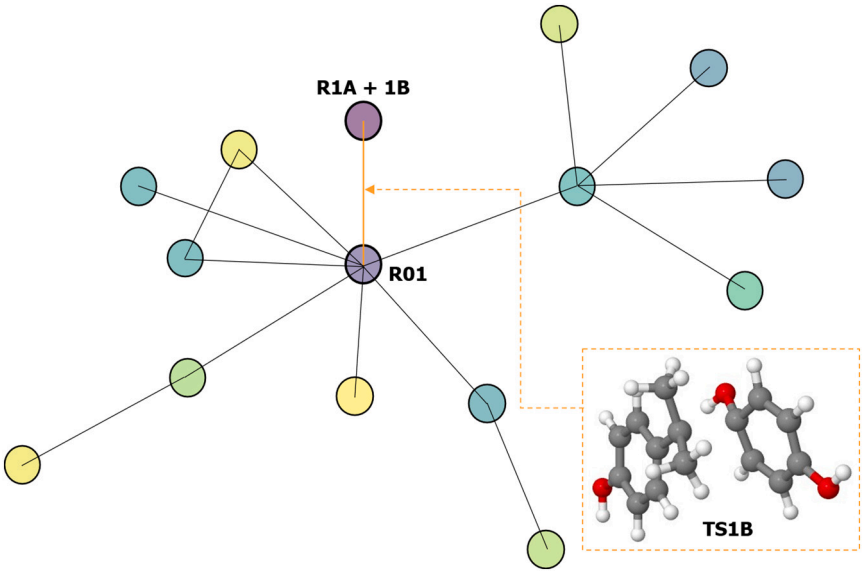

Fig. 2. Illustration (generated with *amk_tools*) of the Level2-calculated RXNet for the unimolecular reactions of the radical intermediate **R01**. The circles (nodes) represent minimum-energy structures, with their colors indicating their energy using the "viridis" colormap, ranging from purple (low energy) to yellow (high energy). The lines (edges) represent pathways connecting pairs of nodes.

radical modeled to mimic a Fenton reaction, where the generation of the OH radical is 17 μM per minute (as determined experimentally, see Section 2.1). The simulations are conducted at a temperature of 298 K. This approach allows for the determination of chemical species concentrations, under the given conditions. These operating conditions were deliberately fixed in order to isolate the intrinsic degradation mechanism without the additional complexity introduced by variables such as pH, temperature, oxidant dosage, or the presence of scavengers. While such parameters are well known to influence kinetics, their systematic exploration lies beyond the scope of the present study. Nevertheless, the computational workflow developed here is readily adaptable to different operating scenarios, providing a flexible framework for future investigations.

In this work, the unimolecular rate coefficients are determined using conventional transition state theory (TST) [71]:

$$k^{\mathrm{TST}}(T) = \sigma \frac{k_B T}{h} e^{-\frac{\Delta G^{\ddagger,o}}{RT}} \tag{2}$$

where σ is the reaction path degeneracy [57], k_B is Boltzmann's constant, T is the temperature, h is Planck's constant, $\Delta G^{\ddagger,o}$ is the standard free energy of activation at a reference concentration $c^o = 1$ M, and R is the gas constant.

In contrast, bimolecular rate coefficients are governed by two consecutive dynamical bottlenecks:

1. A free energy bottleneck (TS1) corresponding to a barrierless association, assumed to be diffusion controlled. The rate coefficient $k_1(T)$ is calculated using the equation [38,72]:

$$k_1(T) = \frac{8 k_B T}{3\eta} \tag{3}$$

where η is the viscosity of the solvent (water in the case studied here).

2. A second bottleneck (TS2) associated to a first-order saddle point. At this stage, conventional TST is applied, with the rate coefficient, $k_2(T)$, given by Eq. (2), where $\Delta G^{\ddagger,o}$ is defined as the difference between the Gibbs free energy of the saddle point and that of the reactants.

For cases involving such dual bottlenecks, the canonical unified statistical (CUS) model [73] is employed to approximate the overall bimolecular rate coefficient k_{bim} as:

$$k_{bim}(T) = \frac{k_1 k_2}{k_1 + k_2} \tag{4}$$

Eq. (4) is referred to by [74] as a correction factor. To avoid unnecessary notational complexity, the standard state symbol on G will be omitted henceforth.

3. Reaction mechanisms

Fig. 3 depicts the obtained degradation mechanism of BPA. Hydroxyl radicals initiate the oxidative degradation of BPA (at the center of the Figure) either by adding directly to a carbon atom (OH-addition) or by abstracting a hydrogen atom (H-abstraction). The radicals produced by these initial reactions with the OH radical are labeled **R01** to **R04** from those arising from OH-addition to BPA, and **R05** to **R07** for those formed through H-abstraction. Notice that these intermediates can further evolve through successive OH attacks, e.g. **R04** + OH → **4A**, or by undergoing molecular rearrangements, e.g. **R01** → **R1A** + **1B**. For clarity, the stable species in Fig. 3 are listed in Table 1 together with their chemical names.

In Fig. 3, unimolecular reactions marked with an "x" symbol have Gibbs free energy barriers (calculated at **Level 3** with SMD correction) above 30 kcal·mol^{-1}, making them essentially inaccessible under our reaction conditions. To determine whether explicit water molecules could lower these barriers, we selectively introduced one or two molecules of solvent and re-optimized the corresponding transition states. This procedure was applied only to rate-determining steps with high-barrier reactions (>30 kcal·mol^{-1}) in order to capture the most relevant hydrogen-bonding and proton transfer effects while keeping the computational effort tractable. In some cases, the effect is dramatic, whereas in others it has little impact. For example, the **5A** → **3B** isomerization barrier drops from 44.5 kcal·mol^{-1} to 28.4 kcal·mol^{-1} by adding one water molecule and to 18.4 kcal·mol^{-1} by adding two (see Fig. 4). By contrast, the **3A** → **3B** barrier barely changes (46.4, 42.0, and 43.5 kcal·mol^{-1} with zero, one, or two water molecules, respectively). While larger hydration clusters or cooperative solvation effects could further modulate barrier heights, a systematic exploration of such scenarios lies beyond the scope of this study. Nevertheless, the selected cases are representative enough to highlight the critical role of explicit solvent molecules in modulating reactivity under aqueous conditions. For all the reactions marked with "x", we used the lowest computed barrier when obtaining the Gibbs free energy profiles and when calculating the corresponding rate constants.

The following two sections provide a detailed analysis of the various degradation pathways identified in this study. To facilitate the

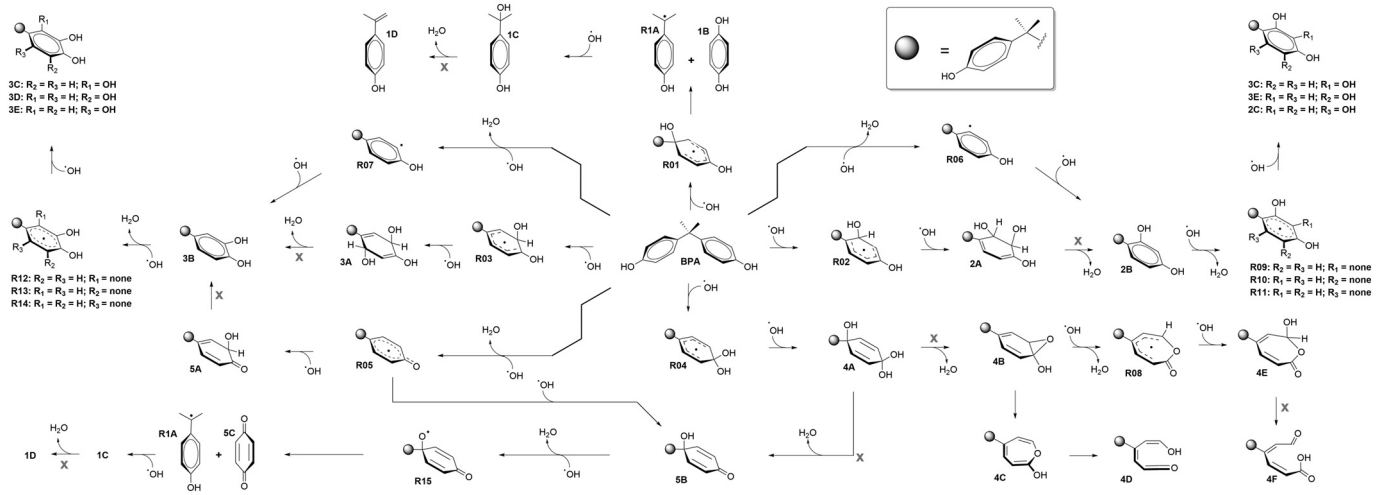

Fig. 3. DFT-computed initial steps of the oxidative degradation of BPA. Paths marked with "x" were also examined by including explicit water molecules.

Table 1
Stable species in the BPA degradation network with their corresponding chemical names. Common names, for some species, are also shown in a second row in italics.

BPA	2,2-bis(4-hydroxyphenyl)propane
	Bisphenol A (or just BPA)
1B	benzene-1,4-diol
	hydroquinone
1C	4-(2-hydroxypropan-2-yl)phenol
	4-hydroxycumyl alcohol
1D	4-(prop-1-en-2-yl)phenol
	p-isopropenylphenol
2A	6-[2-(4-hydroxyphenyl)propan-2-yl]cyclohexa-3,5-diene-1,2,3-triol
2B	4-[2-(4-hydroxyphenyl)propan-2-yl]benzene-1,3-diol
2C	2-[2-(4-hydroxyphenyl)propan-2-yl]benzene-1,3,5-triol
3A	5-[2-(4-hydroxyphenyl)propan-2-yl]cyclohexa-2,5-diene-1,2,4-triol
3B	4-[2-(4-hydroxyphenyl)propan-2-yl]benzene-1,2-diol)
	5-hydroxybisphenol A (or just BPA catechol)
3C	4-(2-(4-hydroxyphenyl)propan-2-yl)benzene-1,2,3-triol
3D	5-[2-(4-hydroxyphenyl)propan-2-yl]benzene-1,2,3-triol
3E	5-(2-(4-hydroxyphenyl)propan-2-yl)benzene-1,2,4-triol
4A	4-[2-(4-hydroxyphenyl)propan-2-yl]cyclohexa-2,5-diene-1,1,4-triol
4B	4-[2-(4-hydroxyphenyl)propan-2-yl]-7-oxabicyclo[4.1.0]hepta-2,4-dien-1-ol
4C	5-[2-(4-hydroxyphenyl)propan-2-yl]oxepin-2-ol
4D	6-hydroxy-4-[2-(4-hydroxyphenyl)propan-2-yl]hexa-1,3,5-trien-1-one
4E	7-hydroxy-5-[2-(4-hydroxyphenyl)propan-2-yl]oxepin-2(7*H*)-one
4F	(2*Z*,4*E*)-4-[2-(4-hydroxyphenyl)propan-2-yl]-6-oxohexa-2,4-dienoic acid
5A	6-hydroxy-4-[2-(4-hydroxyphenyl)propan-2-yl]cyclohexa-2,4-dien-1-one
5B	4-hydroxy-4-[2-(4-hydroxyphenyl)propan-2-yl]cyclohexa-2,5-dien-1-one
5C	cyclohexa-2,5-diene-1,4-dione
	p-benzoquinone

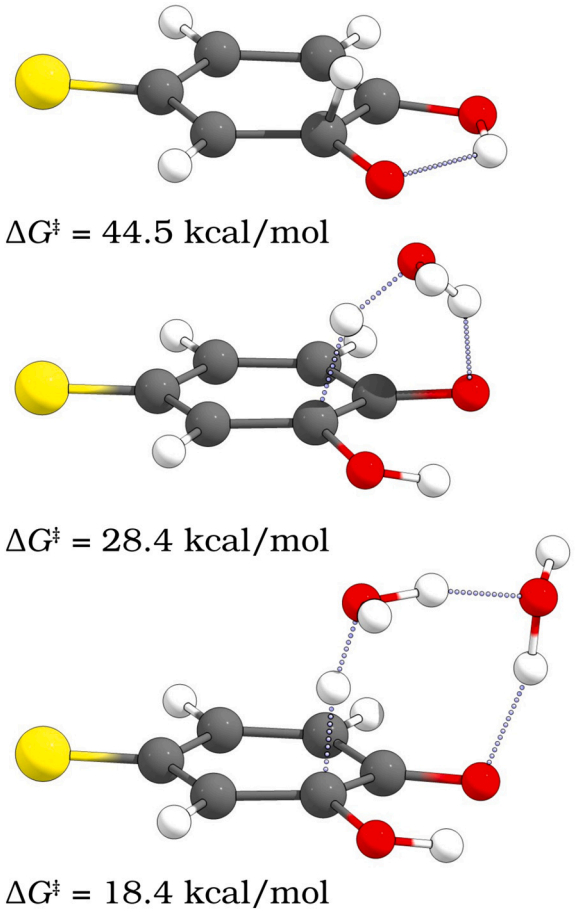

Fig. 4. Transition state structure for the isomerization of **5A** into **3B** without explicit and with explicit water molecules. The yellow sphere represents, similarly to Fig. 3, the HO − C_6H_4 − $C(Me)_2$− fragment.

examination, we have divided our analysis into pathways initiated by OH-addition reactions and those initiated by H-abstraction reactions. Energy profiles, calculated at the ωB97XD/def2-TZVPP level of theory with SMD corrections, for the pathways initiated by OH-addition and H-abstraction, are depicted in Figs. 5 and 6, respectively.

3.1. Pathways initiated by OH-addition reactions

The radical **R01** is formed by the addition of a hydroxyl radical to the *ipso* carbon of BPA, overcoming a Gibbs free-energy barrier of 6.4 kcal·mol^{-1} (Fig. 5, red). *AutoMeKin* then predicts that **R01** rearranges into radical **R1A** and hydroquinone (**1B**) via an 11.6 kcal·mol^{-1} barrier. From **R1A**, a barrierless OH-addition yields tertiary alcohol **1C**, 4-(2-hydroxypropan-2-yl)phenol. Although **1C** could theoretically dehydrate to olefin **1D,** 4-(prop-1-en-2-yl)phenol, our searches failed to locate any viable pathway (its lowest Gibbs barrier remains 52.6 kcal·mol^{-1}) so the **R01** branch would terminate at **1C** and **1B**.

In parallel, OH-addition to the *ortho* and *meta* positions produces radicals **R02** (5.5 kcal·mol^{-1} barrier) and **R03** (2.6 kcal·mol^{-1} barrier); each undergoes a second barrierless OH-addition to give enolic intermediates **2A** and **3A**, respectively (Fig. 5, blue and green). From these enols, the most favorable next step, according to *AutoMekin*, is dehydration to restore aromaticity, giving monohydroxylated BPA derivatives **2B** and **3B**. These two intermediates would then undergo aromatic H-abstraction by OH—barriers are low (between 9 and 11 kcal·mol^{-1}, except the path to **3D** at 25.6 kcal·mol^{-1})—and the resulting radicals react barrierlessly with OH, leading to the formation of the trihydroxylated benzene-ring species **2C**, **3C**, **3D**, and **3E**.

The **R04** branch begins when OH adds to the *para* carbon of BPA (5.3 kcal·mol^{-1} barrier, Fig. 5, black), followed by a barrierless OH-addition at the *ipso* carbon to produce the ketal **4A**. From **4A**, two pathways open:

- a 1,6-hydrogen migration from the ketal hydroxyl to the OH at the *ipso* carbon to release H_2O and generate epoxide **4B**, or
- a rearrangement of the ketal group to yield ketone **5B** plus H_2O.

Epoxide **4B**'s ring strain drives two possible routes. On the one side, a unimolecular rearrangement to antiaromatic **4C** (9.9 kcal·mol^{-1} barrier) and a subsequent ring opening to ketene **4D**. On the other side, OH can abstract the hydroxyl hydrogen of **4B**, forming ε-caprolactonic radical **R08**, which then undergoes barrierless OH-addition to give ε-caprolactone **4E**. The isomerization of **4E** generates carboxylic acid **4F**. We highlight here the importance of including explicit water molecules. One water molecule lowers the **4C** → **4D** barrier from 38.5 to 24.7 kcal·mol^{-1}; regarding **4E** → **4F**, two explicit water molecules lower its barrier from 36.2 to 14.4 kcal·mol^{-1}.

Ketone **5B** can also undergo H-abstraction by OH (14.8 kcal·mol^{-1} barrier) to form radical **R15**, which fragments into **R1A** and *p*-benzoquinone (**5C**). **R1A** follows the same barrierless OH-addition to **1C** as in the **R01** branch.

Although the **R02** and **R03** branches formally connect to trihydroxylated benzene-ring species, the dehydration steps from **2A** and **3A** are highly endergonic (barriers >40 kcal·mol^{-1}), even after considering explicit water molecules. As a result, under the studied conditions these pathways are effectively terminated at **2A** and **3A** and do not progress further to **2B** and **3B**. Likewise, dehydration of **4A** to form either **4B** or **5B** involves high energy barriers (39.9 and 29.4 kcal·mol^{-1}, respectively), so the **R04** pathway also terminates at **4A**. Therefore, while the **R02**, **R03**, and **R04** branches are theoretically connected to trihydroxylated benzene-ring products, they remain kinetically blocked at earlier intermediates, which can still play a significant role in the overall degradation mechanism.

3.2. Pathways initiated by H-abstraction reactions

Among the three H abstraction routes (Fig. 6), the formation of **R05**,

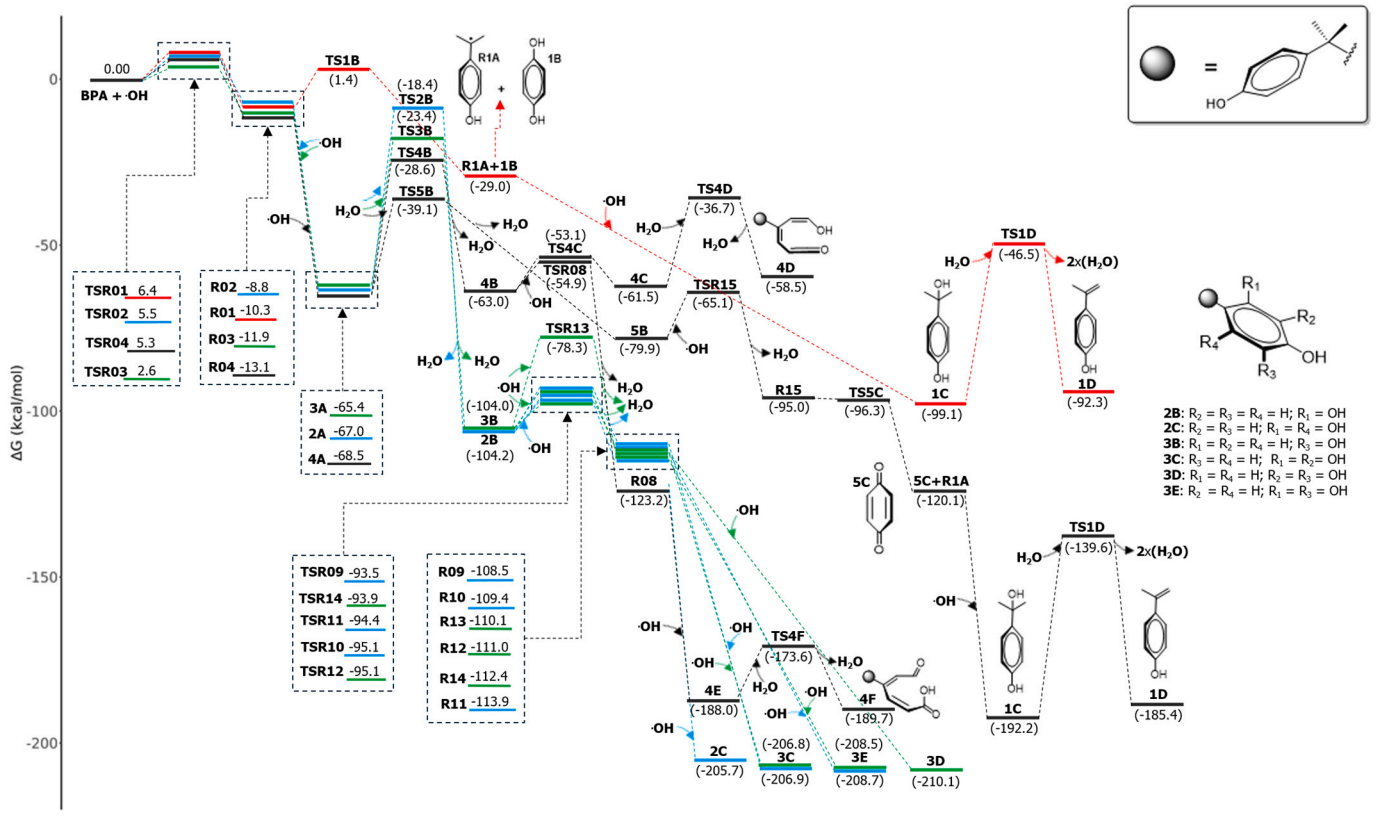

Fig. 5. DFT-calculated Gibbs free energy profiles for the reaction pathways associated with initial the addition of OH to BPA. A color code is used to distinguish the addition of OH to the four different carbon atoms in the phenolic ring: *ipso* (red), *ortho* (blue), *meta* (green), and *para* (black).

by abstracting the hydroxylic hydrogen, is the most favorable pathway (with a barrier of only 0.8 kcal·mol^{-1}). From **R05**, OH can add at the *meta* or at the *ipso* positions to form ketones **5A** and **5B**, respectively. Interestingly, ketone **5A** can rearrange to intermediate **3B**. Although this step has a prohibitively high barrier of 44.5 kcal·mol^{-1} under implicit-solvent conditions, it becomes feasible when two explicit water molecules are included (the barrier lowers to 18.4 kcal·mol^{-1}).

The remaining H-abstractions, at the *ortho* and *meta* positions, lead to **R06** and **R07** radical species, respectively. These steps have the highest energy barriers among the seven primary radical formations (between 8 and 10 kcal·mol^{-1}), which diminishes their significance. The subsequent barrierless OH-addition from them would form intermediates **2B** and **3B**, respectively.

The subsequent transformations of **2B**, **3B** and **5B** have been already described in the previous section.

3.3. Literature validation of predicted intermediates

Although our computational results just focus on the initial stages of BPA degradation, it is noteworthy that several products previously mentioned (and shown in Fig. 3) have been reported in previous works:

a) Compounds **1B**, **1C**, and **5C** [22–24,26,27,75–86].
b) Compounds **2B** [24,79–81,87] and **3B** [21,23,24,76,79–82,84, 87–90]. Although both compounds are commonly observed as intermediates, **3B** has been reported more frequently, which is consistent with the findings of our kinetic study described below.
c) Compounds **2C**, **3C**, and **3E** [22,75,80,81,91].

It is also worth noting that, in most cases, the experimental reports of BPA degradation intermediates are qualitative, which precludes a direct quantitative comparison with our simulations presented in the next section.

4. Kinetic modeling results

Kinetic Monte Carlo (KMC) simulations were carried out with *Pilgrim* to quantify the likelihood of each reaction channel in the proposed degradation mechanism and to determine the predominant product distribution. Two kinetic regimes were explored to assess how the OH radical concentration affects BPA conversion. In both situations, the initial concentration of BPA was set to 1.31 μM.

4.1. Fixed [BPA]:[OH] ratios and mechanism reduction

In the first set of simulations, we varied the initial [OH]:[BPA] ratio from 0:1 to 5:1 (Fig. 7) and monitored each run for 90 min—long enough for all species to reach steady-state concentrations. BPA degradation proved highly sensitive to [OH] and complete conversion required at least a 2:1 ratio. Below this threshold, intermediates **3A**, **3B**, and **5B** dominate, with secondary accumulation of **4A** and **2A**, highlighting the main mechanistic branches. Once the [OH]:[BPA] ratio exceeds 2:1, **3B** disappears as it is rapidly converted into the trihydroxylated species **3C** under OH excess. Likewise, **5B** is consumed to yield cleavage products **5C** and **1C** via C—C bond scission in **R15** radical. All other species exhibit final concentrations below 0.04 μM—i.e., less than 3 % of the initial BPA concentration. These results align with our mechanistic analysis. It is interesting to note that the **3B** is produced via the H-abstraction route (**R05** → **5A** → **3B**) rather than through OH-addition (**R03** → **3A** → **3B**). Similarly, **5B** forms from **R05** (**R05** → **5B**) and not from the **R04** branch (**R04** → **4A** → **5B**).

To identify the core reactions in Fig. 3, we ran N separate KMC simulations, each omitting one of the N elementary steps (so every run contained $N - 1$ reactions). We then compared the profile from each truncated network to that of the full mechanism (i.e. that in Fig. 7). Any reaction whose removal altered any species' concentration by more than 3 % of the initial BPA level (i.e., > 0.04 μM) was marked as essential.

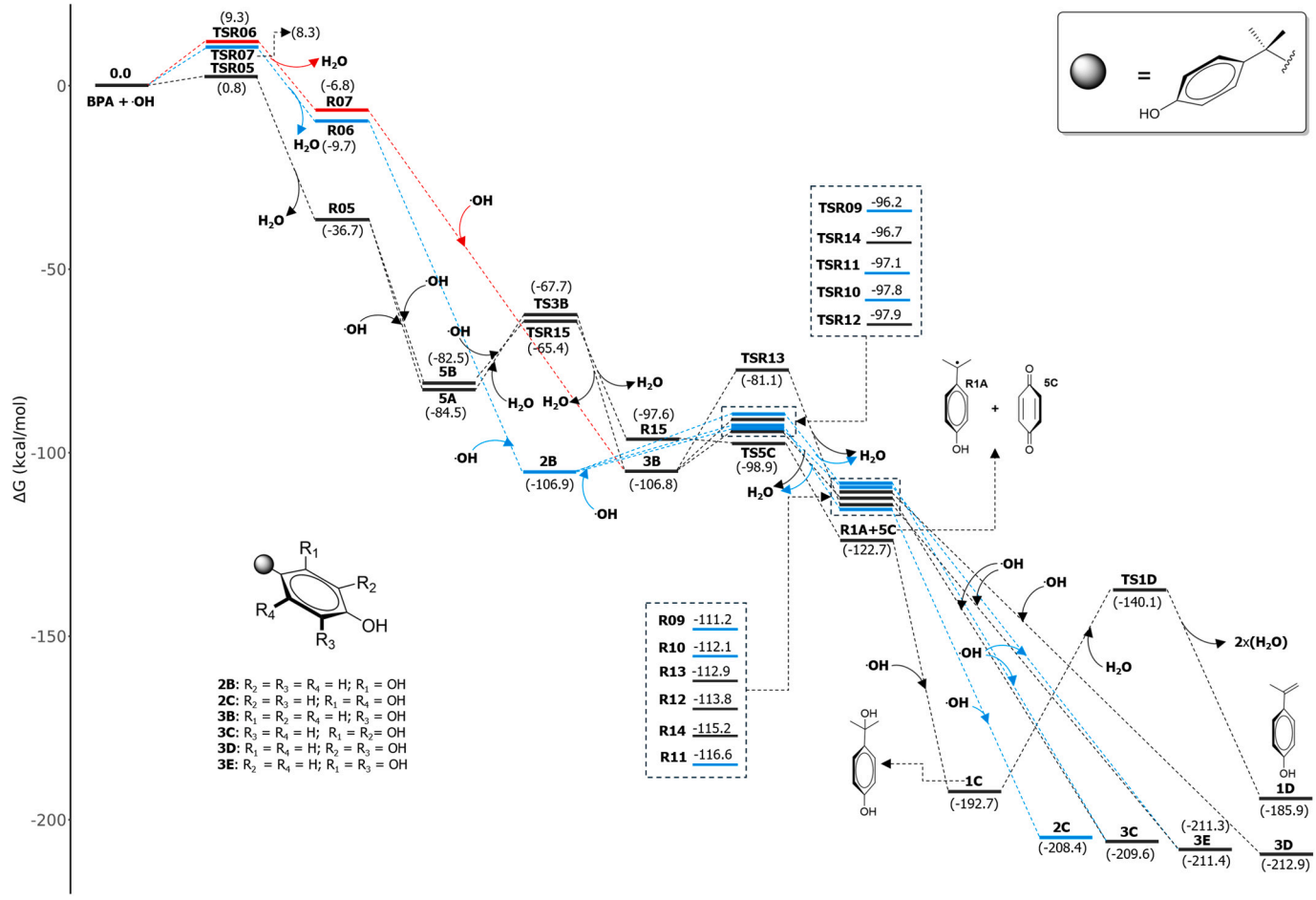

Fig. 6. DFT-calculated Gibbs free energy profiles for the reaction pathways associated with the initial H-abstraction reactions. A color code is used to distinguish the pathways related to the removal of hydrogen from different positions.

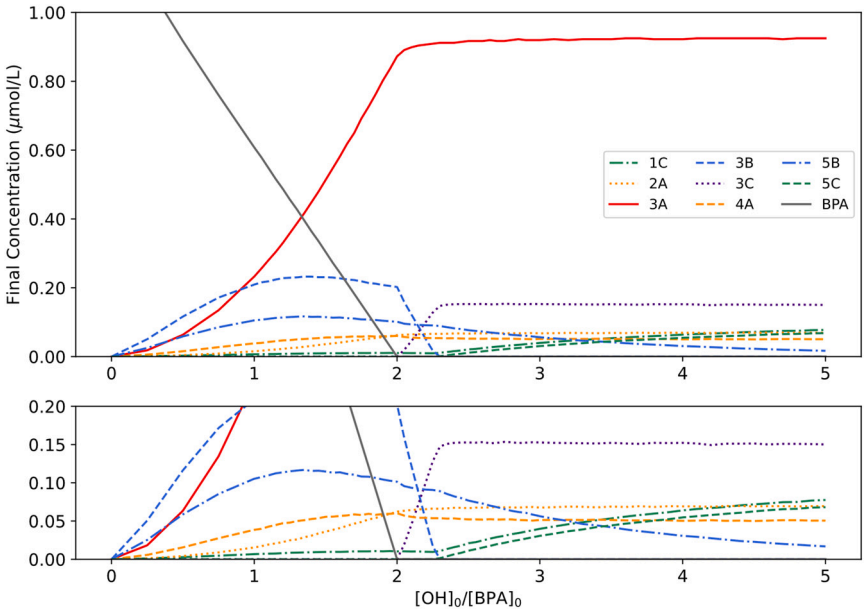

Fig. 7. Final concentrations of the key species plotted against the initial [OH]:[BPA] ratio (radical species omitted). The lower panel provides a zoomed-in view of the upper panel.

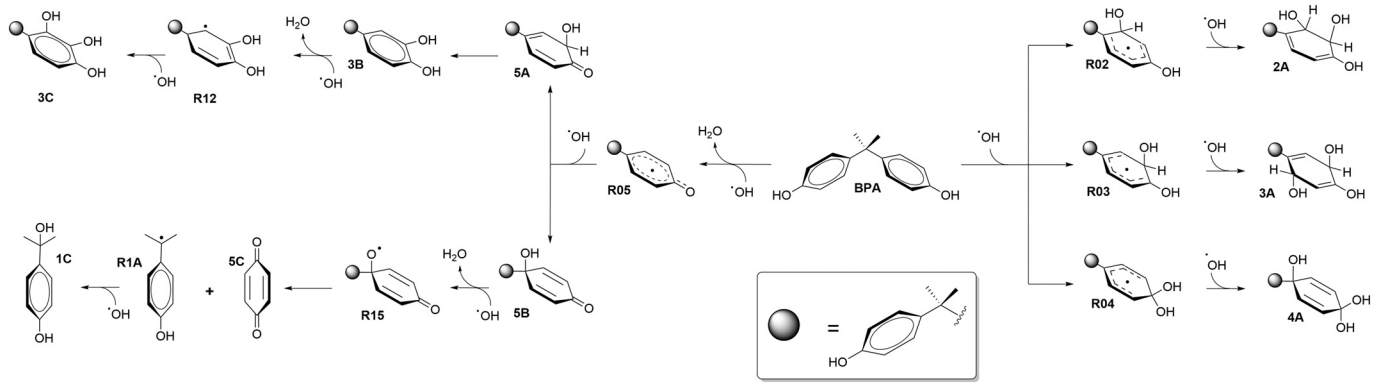

Fig. 8. Reduced mechanism for the initial steps of the oxidative degradation of BPA.

Using this threshold yielded the reduced mechanism shown in Fig. 8, containing only the essential steps necessary to reproduce the full-network kinetics.

In the reduced mechanism, OH-radical chemistry is significantly simplified: every OH-addition pathway—except the *ipso*-addition, which was removed—is limited to a two-step process terminating in the trihydroxylated compounds (**2A**, **3A** and **4A**). Of the three possible H-abstraction routes, only the abstraction of the hydroxylic hydrogen (**R05**) persists. These results are consistent with our analysis of the energy profiles.

Regarding the influence of the threshold value in the simplified mechanism, a sensitivity analysis was carried out: 19 reactions were retained with a cutoff of 0.01 μM, 17 with 0.02–0.03 μM, 15 with 0.04–0.06 μM, but the number dropped sharply to 9 at 0.07 μM and to only 5 at 0.16–0.20 μM. Importantly, for thresholds up to 0.06 μM, the reduced networks reproduced the same dominant products and mechanistic picture, whereas larger cutoffs eliminated essential branches. This demonstrates that the simplified mechanism presented here is robust with respect to reasonable variations of the cutoff criterion.

4.2. Fenton-mimicking conditions

We also simulated a Fenton-type scenario by starting with zero OH radical concentration and increasing it at a rate of 17 μM·min^{-1}. The results, shown in Fig. 9, indicate that the reaction reaches completion in about 10 min, which is consistent with the experimentally reported range of 1–60 min [76,77,86,87].

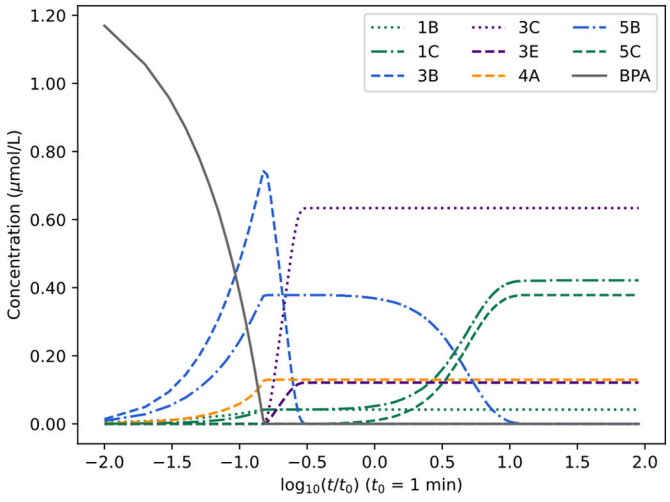

Fig. 9. Time profiles for the key degradation products under Fenton-like conditions (radical species omitted) using the whole mechanism. The abscissa is plotted on a base-10 logarithmic scale for improved visualization (time in minutes).

We observe that the temporal evolution closely parallels the fixed-ratio results of Fig. 7: at low [OH] (early times), intermediates **3B** and **5B** accumulate, but both are consumed as [OH] rise (later times). Specifically, **3B** is converted into the trihydroxylated species **3C**, with its concentration dropping after approximately 0.15 min. This time point corresponds to an in situ [OH] of about 2.60 μM – equivalent to a 2:1 [OH]:[BPA] ratio and, hence, consistent with our earlier findings. After **3B** is fully depleted, **5B** cleaves to form **5C** and **1C**. The slightly higher concentration of **1C** versus **5C** arises from the additional formation pathway through radical **R01**. Finally, other trihydroxylated products, such as **3E** and **4A**, begin to accumulate at later times.

Despite the overall parallels between the two simulation regimes, a striking contrast emerges in the behavior of intermediate **3A** (Figs. 7 and 9). In the fixed-ratio simulations, **3A** accumulates as the initial [OH] increases, but it remains essentially undetectable under the Fenton-mimicking ramp-up.

When [OH] rises slowly (*Fenton conditions*), neither **R03** nor **R05** can proceed any further after their formation, as there is not enough [OH] for the subsequent addition. Due to that, the system is initially under thermodynamic control, favoring formation of the more stable radical **R05** (ΔG = –36.7 kcal·mol^{-1}) over **R03** (ΔG = –11.9 kcal·mol^{-1}): i.e. their concentrations establish a pseudo-equilibrium. Once [OH] becomes sufficient to drive the addition, only **R05** has a significant concentration and, consequently, the reaction flux proceeds predominantly via **R05** (to **5A** and to **5B**), rather than via **R03** (to **3A**). Thus, this mechanism prevents any measurable buildup of **3A** during ramp-up.

By contrast, when [OH] is high enough from the beginning (t = 0), both **R03** and **R05** immediately undergo barrierless, diffusion-limited OH addition. This converts **R03** into **3A**, and **R05** into **5A** and **5B**. Once formed, **3A** accumulates because the reverse reaction that regenerates **R03** (ΔG = +53.5 kcal·mol^{-1}) and its dehydration to **3B** (ΔG = +34.3 kcal·mol^{-1}) are extremely slow.

Finaly, simulations with the reduced mechanism yield virtually identical concentration–time profiles, demonstrating that it captures all essential Fenton-condition chemistry. The only notable deviations are that, with the *ipso*-addition pathway removed, **5C** and **1C** now accumulate to equal levels, and the trihydroxylated product **3E** is no longer formed.

5. Conclusions

In this study, we combined automated reaction-discovery (*AutoMeKin*) with first-principles rate-constant calculations (*Pilgrim*) to construct a thorough, unbiased kinetic map of BPA degradation under Fenton-type conditions. Extensive DFT-level exploration of the potential-energy surface revealed every plausible OH-addition and H-abstraction pathway, producing a detailed reaction network of ring-opening,

hydroxylation, and rearrangement steps. This reaction mechanism workflow should be regarded as semi-automated: while unimolecular reactivity is explored in a fully automated manner, the manual setup of certain bimolecular and solvent-assisted processes remains necessary, as no general automated protocol currently exists for these cases. Overcoming this limitation constitutes an important avenue for future methodological development.

Starting from fixed [OH]:[BPA] ratios, we applied a one-at-a-time reaction sensitivity protocol to pare down the full network (*N* reactions) into a minimal mechanism. In this reduced scheme, each OH-addition pathway ends once the trihydroxylated species is reached (except for the addition at the *ipso* position, which is removed). Of the various H-abstraction channels, only the abstraction of the phenolic O—H remains.

Both the complete and the pared-down mechanisms were evaluated under Fenton-mimicking conditions, in which [OH] is generated in situ at 17 μM min^{-1}. Each model produces virtually identical concentration–time profiles: **3B** and **5B** build up initially, but as [OH] surpasses the 2:1 threshold, **3B** is converted into the trihydroxylated product **3C**, while **5B** undergoes C—C bond scission (following OH addition) to yield **1C** and **5C**. Notably, the intermediate **3A**—readily observed under fixed-ratio simulations—remains essentially undetectable during ramp-up, reflecting the thermodynamic preference for **R05** formation and the brief window for **3A** generation.

A key novelty of this work lies in the combination of automated reaction discovery with kinetic Monte Carlo simulations, which allows not only the systematic identification of degradation pathways but also the construction of a predictive kinetic model. This integrated approach reduces human bias, improves computational efficiency, and offers clear advantages over conventional methodologies that rely solely on static quantum-chemical calculations or empirical kinetics. Its transferability makes it a powerful framework for guiding the rational design of advanced oxidation processes for other organic pollutants.

CRediT authorship contribution statement

Pablo A. Chacón-Morales: Writing – original draft, Validation, Investigation, Data curation. **Antonio Fernández-Ramos:** Writing – review & editing, Software, Methodology. **Jorge González-Rodríguez:** Writing – review & editing, Investigation. **María Teresa Moreira:** Writing – review & editing. **Emilio Martínez-Núñez:** Writing – original draft, Software, Methodology, Conceptualization. **David Ferro-Costas:** Writing – review & editing, Validation, Supervision, Software, Methodology, Investigation, Data curation, Conceptualization.

Declaration of competing interest

The authors declare that they have no known competing financial interests or personal relationships that could have appeared to influence the work reported in this paper.

Acknowledgements

M.T.M. acknowledges support from the CIES project (PID2022-142334OB-I00), funded by MICIU/AEI/10.13039/501100011033 and FEDER, EU. A.F.-R., E.M.-N. and M.T.M. acknowledge support from the SPOTLIGHT project (PDC2021-121540-I00), funded by MICIU/AEI/10.13039/501100011033 and the European Union NextGenerationEU/PRTR. A.F.-R., D.F.-C., E.M.-N., and J.G.-R. acknowledge financial support from the Consellería de Educación, Ciencia, Universidades e Formación Profesional (Xunta de Galicia): A.F.-R., D.F.-C. and E.M.-N through the *Grupo de referencia competitiva* grant (ED431C 2025/06); A.F.-R. through the *Centro singular de Investigación de Galicia* accreditation 2023-2027 (ED431G 2023/03), co-funded by the European Regional Development Fund (ERDF); and J.G.-R. through his postdoctoral fellowship (ED481B-2025/070). We also thank the Galician Supercomputer Center (CESGA) for providing access to their computational resources.

Appendix A. Supplementary data

Supplementary data to this article can be found online at https://doi.org/10.1016/j.cej.2025.169248.

Data availability

Data can be found in Zenodo repository. Extra data can be available if requested.

References

[1] C. Zhang, X. Wang, Z. Ma, Z. Luan, Y. Wang, Z. Wang, L. Wang, Removal of phenolic substances from wastewater by algae. A review, Environ. Chem. Lett. 18 (2020) 377–392, https://doi.org/10.1007/s10311-019-00953-2.

[2] Z. Duan, L. Zhu, L. Zhu, Y. Kun, X. Zhu, Individual and joint toxic effects of pentachlorophenol and bisphenol A on the development of zebrafish (*Danio rerio*) embryo, Ecotoxicol. Environ. Saf. 71 (2008) 774–780, https://doi.org/10.1016/j.ecoenv.2008.01.021.

[3] K. Czarny, D. Szczukocki, B. Krawczyk, M. Zieliński, E. Miękoś, R. Gadzała-Kopciuch, The impact of estrogens on aquatic organisms and methods for their determination, Crit. Rev. Environ. Sci. Technol. 47 (2017) 909–963, https://doi.org/10.1080/10643389.2017.1334458.

[4] T. Ding, W. Li, M. Yang, B. Yang, J. Li, Toxicity and biotransformation of bisphenol S in freshwater green alga *Chlorella vulgaris*, Sci. Total Environ. 747 (2020) 141144, https://doi.org/10.1016/j.scitotenv.2020.141144.

[5] B.S. Rubin, Bisphenol A: an endocrine disruptor with widespread exposure and multiple effects, J. Steroid Biochem. Mol. Biol. 127 (2011) 27–34, https://doi.org/10.1016/j.jsbmb.2011.05.002.

[6] Q. Chen, C. Zhou, W. Shi, X. Wang, P. Xia, M. Song, J. Liu, H. Zhu, X. Zhang, S. Wei, H. Yu, Mechanistic *in silico* modeling of bisphenols to predict estrogen and glucocorticoid disrupting potentials, Sci. Total Environ. 728 (2020) 138854, https://doi.org/10.1016/j.scitotenv.2020.138854.

[7] J. González-Rodríguez, J.J. Conde, Z. Vargas-Osorio, C. Vázquez-Vázquez, Y. Piñeiro, J. Rivas, G. Feijoo, M.T. Moreira, LED-driven photo-Fenton process for micropollutant removal by nanostructured magnetite anchored in mesoporous silica, J. Environ. Manage. 349 (2024) 119461, https://doi.org/10.1016/j.jenvman.2023.119461.

[8] B. Jiang, Y. Zhang, C. Li, J. Guo, C. Sun, Zero-valent iron loaded on N-doped biochar fabricated by one-step pyrolysis of K_2FeO_4 and coffee grounds as a persulfate activator for bisphenol A degradation, Process. Saf. Environ. Prot. 170 (2023) 328–338, https://doi.org/10.1016/j.psep.2022.11.081.

[9] L. Wang, T. Luo, J. Jiao, G. Liu, B. Liu, L. Liu, Y. Li, One-step modification of MIL-88A(Fe) enhanced electro-Fenton coupled membrane filtration system for the removal of bisphenol a, Sep. Purif. Technol. 329 (2024) 125091, https://doi.org/10.1016/j.seppur.2023.125091.

[10] W. Huang, H. Ming, X. Bian, C. Yang, Y. Hou, K. Ding, J. Zhang, Copper single atoms incorporated in crystalline carbon nitride for efficient photocatalytic activation of peroxymonosulfate toward bisphenol a removal with visible light, Chem. Eng. J. 473 (2023) 145230, https://doi.org/10.1016/j.cej.2023.145230.

[11] Y. Yang, F. Zhao, L. Yang, J. Zhang, H.-D. Park, Z. Li, H. Chen, X. Zhang, M. Gao, Catalytic degradation of bisphenol a (BPA) in water by immobilizing silver-loaded graphene oxide (GO-ag) in ultrafiltration membrane with finger-like structure, Chem. Eng. J. 474 (2023) 145577, https://doi.org/10.1016/j.cej.2023.145577.

[12] J. Yu, W. Qiu, X. Lin, Y. Wang, X. Lu, Y. Yu, H. Gu, S. Heng, H. Zhang, J. Ma, Periodate activation with stable $MgMn_2O_4$ spinel for bisphenol a removal: radical and non-radical pathways, Chem. Eng. J. 459 (2023) 141574, https://doi.org/10.1016/j.cej.2023.141574.

[13] J. Dai, Z. Wang, K. Chen, D. Ding, S. Yang, T. Cai, Applying a novel advanced oxidation process of biochar activated periodate for the efficient degradation of bisphenol a: two nonradical pathways, Chem. Eng. J. 453 (2023) 139889, https://doi.org/10.1016/j.cej.2022.139889.

[14] E. Neyens, J. Baeyens, A review of classic Fenton's peroxidation as an advanced oxidation technique, J. Hazard. Mater. 98 (1) (2003) 33–50, https://doi.org/10.1016/S0304-3894(02)00282-0.

[15] X. Fan, J.B. McLaughlin, A. Melman, S. Mededovic Thagard, Quantum chemical approach for determining degradation pathways of phenol by electrical discharge plasmas, Plasma Chem. Plasma Process. 37 (2017) 5–28, https://doi.org/10.1007/s11090-016-9758-6.

[16] Q. Mei, H. Cao, D. Han, M. Li, S. Yao, J. Xie, J. Zhan, Q. Zhang, W. Wang, M. He, Theoretical insight into the degradation of *p*-nitrophenol by OH radicals synergized with other active oxidants in aqueous solution, J. Hazard. Mater. 389 (2020) 121901, https://doi.org/10.1016/j.jhazmat.2019.121901.

[17] Y. Chen, Y. Yang, J. Cui, H. Zhang, Y. Zhao, Decoding PFAS contamination via Raman spectroscopy: a combined DFT and machine learning investigation, J. Hazard. Mater. 465 (2024) 133260, https://doi.org/10.1016/j.jhazmat.2023.133260.

[18] A.K. Ilango, P. Arathala, R.A. Musah, Y. Liang, Experimental and density functional theory investigation of surface-modified biopolymer for improved adsorption of

mixtures of per- and polyfluoroalkyl substances in water, Water Res. 255 (2024) 121458, https://doi.org/10.1016/j.watres.2024.121458.
[19] Z. Xiao, B. Yang, X. Feng, Z. Liao, H. Shi, W. Jiang, C. Wang, N. Ren, Density functional theory and machine learning-based quantitative structure–activity relationship models enabling prediction of contaminant degradation performance with heterogeneous peroxymonosulfate treatments, Environ. Sci. Technol. 57 (2023) 3951–3961, https://doi.org/10.1021/acs.est.2c09034.
[20] M. Umar, H. Khan, S. Hussain, M. Arshad, H. Choi, E.C. Lima, Integrating DFT and machine learning for the design and optimization of sodium alginate-based hydrogel adsorbents: efficient removal of pollutants from wastewater, Environ. Res. 247 (2024) 118219, https://doi.org/10.1016/j.envres.2024.118219.
[21] N. Jiang, X. Li, H. Guo, J. Li, K. Shang, N. Lu, Y. Wu, Plasma-assisted catalysis decomposition of BPA over graphene-CdS nanocomposites in pulsed gas-liquid hybrid discharge: Photocorrosion inhibition and synergistic mechanism analysis, Chem. Eng. J. 412 (2021) 128627, https://doi.org/10.1016/j.cej.2021.128627.
[22] W. Zhao, B. Zhou, Assessing the role of CNTs in H_2O_2/Fe(III) Fenton-like process: mechanism, DFT calculations and ecotoxicity evaluation, Sep. Purif. Technol. 259 (2021) 118218, https://doi.org/10.1016/j.seppur.2020.118218.
[23] J. Ding, L. Shen, R. Yan, S. Lu, Y. Zhang, X. Zhang, H. Zhang, Heterogeneously activation of H_2O_2 and persulfate with goethite for bisphenol a degradation: a mechanistic study, Chemosphere 261 (2020) 127715, https://doi.org/10.1016/j.chemosphere.2020.127715.
[24] F. Liu, Q. Dong, C. Nie, Z. Li, B. Zhang, P. Han, W. Yang, M. Tong, Peroxymonosulfate enhanced photocatalytic degradation of serial bisphenols by metal-free covalent organic frameworks under visible light irradiation: mechanisms, degradation pathway and DFT calculation, Chem. Eng. J. 430 (2022) 132833, https://doi.org/10.1016/j.cej.2021.132833.
[25] Q. Han, M. Wang, F. Sun, B. Yu, Z. Dong, P. Li, J. Luo, M. Li, X. Jin, Z. Dai, Effectiveness and degradation pathways of bisphenol a (BPA) initiated by hydroxyl radicals and sulfate radicals in water: initial reaction sites based on DFT prediction, Environ. Res. 216 (2023) 114601, https://doi.org/10.1016/j.envres.2022.114601.
[26] T.-T. Cao, H. Cui, D.-D. Zhou, X. Ren, C.-W. Cui, Degradation mechanism of BPA under VUV irradiation: efficiency contribution and DFT calculations, Environ. Sci. Pollut. Res. 30 (2023) 12813–12824, https://doi.org/10.1007/s11356-022-22893-1.
[27] K. Makarova, E. Olchowik-Grabarek, K. Drabikowski, J. Kurkowiak, K. Zawada, Products of bisphenol a degradation induce cytotoxicity in human erythrocytes (in vitro), Int. J. Mol. Sci. 24 (2023) 492, https://doi.org/10.3390/ijms24010492.
[28] J. Lai, P. Xiao, Y. Li, S. Cui, J. Yang, H. Lian, Visible light and iodate/iodide mediated degradation of bisphenol a by self-assembly 3D hierarchical $BiOIO_3$/Bi_5O_7I Z-scheme heterojunction: intermediates identification, radical mechanism and DFT calculation, J. Hazard. Mater. 448 (2023) 130908, https://doi.org/10.1016/j.jhazmat.2023.130908.
[29] J. Wang, M. Zheng, Y. Deng, M. Liu, Y. Chen, N. Gao, E. Du, W. Chu, H. Guo, Generality and diversity on the kinetics, toxicity and DFT studies of sulfate radical-induced transformation of BPA and its analogues, Water Res. 219 (2022) 118506, https://doi.org/10.1016/j.watres.2022.118506.
[30] E. Martínez-Núñez, G.L. Barnes, D.R. Glowacki, S. Kopec, D. Peláez, A. Rodríguez, R. Rodríguez-Fernández, R.J. Shannon, J.J.P. Stewart, P.G. Tahoces, S.A. Vazquez, AutoMeKin2021: an open-source program for automated reaction discovery, J. Comput. Chem. 42 (2021) 2036–2048, https://doi.org/10.1002/jcc.26734.
[31] D. Ferro-Costas, D.G. Truhlar, A. Fernández-Ramos, Pilgrim: a thermal rate constant calculator and a chemical kinetics simulator, Comput. Phys. Commun. 256 (2020) 107457, https://doi.org/10.1016/j.cpc.2020.107457.
[32] D.T. Gillespie, A general method for numerically simulating the stochastic time evolution of coupled chemical reactions, J. Comput. Phys. 22 (1976) 403–434, https://doi.org/10.1016/0021-9991(76)90041-3.
[33] L. Guerrero-Méndez, A. Lema-Saavedra, E. Jiménez, A. Fernández-Ramos, E. Martínez-Núñez, Gas-phase formation of glycolonitrile in the interstellar medium, Phys. Chem. Chem. Phys. 25 (2023) 20988–20996, https://doi.org/10.1039/D3CP02379F.
[34] B. Ballotta, T.D. Marforio, S. Rampino, E. Martínez-Núñez, V. Barone, M. Melosso, A. Bottoni, L. Dore, Toward the detection of cyanoketene in the interstellar medium: new hints from quantum chemistry and rotational spectroscopy, ACS Earth Space Chem. 7 (2023) 1172–1180, https://doi.org/10.1021/acsearthspacechem.3c00060.
[35] M.J. Wilhelm, E. Martínez-Núñez, J. González-Vázquez, S.A. Vázquez, J.M. Smith, H.-L. Dai, Is photolytic production a viable source of HCN and HNC in astrophysical environments? A laboratory-based feasibility study of methyl cyanoformate, Astrophys. J. 849 (2017) 15, https://doi.org/10.3847/1538-4357/aa8ea7.
[36] M. Castiñeira Reis, E. Martínez Núñez, A. Fernández Ramos, Comprehensive computational automated search of barrierless reactions leading to the formation of benzene and other C_6-membered rings, Sci. Adv. 10 (2024) eadq4077, https://doi.org/10.1126/sciadv.adq4077.
[37] J. Laranjeira, K. Strutyński, L. Marques, E. Martínez-Núñez, M. Melle-Franco, C_{60}+C_{60} molecular bonding revisited and expanded, Carbon 213 (2023) 118209, https://doi.org/10.1016/j.carbon.2023.118209.
[38] J.A. Varela, S.A. Vázquez, E. Martínez-Núñez, An automated method to find reaction mechanisms and solve the kinetics in organometallic catalysis, Chem. Sci. 8 (2017) 3843–3851, https://doi.org/10.1039/C7SC00549K.
[39] F.F. da Silva, T. Cunha, A. Rebelo, A. Gil, M.J. Calhorda, G. García, O. Ingólfsson, P. Limão-Vieira, Electron-transfer-induced side-chain cleavage in tryptophan facilitated through potassium-induced transition-state stabilization in the gas phase, J. Phys. Chem. A 125 (2021) 2324–2333, https://doi.org/10.1021/acs.jpca.1c00690.
[40] E. Rossich Molina, J.-Y. Salpin, R. Spezia, E. Martínez-Núñez, On the gas phase fragmentation of protonated uracil: a statistical perspective, Phys. Chem. Chem. Phys. 18 (2016) 14980–14990, https://doi.org/10.1039/C6CP01657J.
[41] V. Macaluso, D. Scuderi, M.E. Crestoni, S. Fornarini, D. Corinti, E. Dalloz, E. Martinez-Nunez, W.L. Hase, R. Spezia, L-cysteine modified by S-sulfation: consequence on fragmentation processes elucidated by tandem mass spectrometry and chemical dynamics simulations, J. Phys. Chem. A 123 (2019) 3685–3696, https://doi.org/10.1021/acs.jpca.9b01779.
[42] D. Ferro-Costas, E. Martínez-Núñez, J. Rodríguez-Otero, E. Cabaleiro-Lago, C. M. Estévez, B. Fernández, A. Fernández-Ramos, S.A. Vázquez, Influence of multiple conformations and paths on rate constants and product branching ratios. Thermal decomposition of 1-propanol radicals, J. Phys. Chem. A 122 (2018) 4790–4800, https://doi.org/10.1021/acs.jpca.8b02949.
[43] Y. Fenard, A. Gil, G. Vanhove, H.-H. Carstensen, K.M. Van Geem, P. R. Westmoreland, O. Herbinet, F. Battin-Leclerc, A model of tetrahydrofuran low-temperature oxidation based on theoretically calculated rate constants, Combust. Flame 191 (2018) 252–269, https://doi.org/10.1016/j.combustflame.2018.01.006.
[44] R.A. Jara-Toro, G.A. Pino, D.R. Glowacki, R.J. Shannon, E. Martínez-Núñez, Enhancing automated reaction discovery with boxed molecular dynamics in energy space, ChemSystemsChem 2 (2020) e1900024, https://doi.org/10.1002/syst.201900024.
[45] E. Martinez-Nunez, Publications Utilizing AutoMeKin since 2021, https://emartineznunez.github.io/AutoMeKin/docs/works.html (accessed September 2025).
[46] W. Siebrand, Z. Smedarchina, D. Ferro-Costas, E. Martínez-Núñez, A. Fernández-Ramos, Reply to the 'Comment on "Methanol dimer formation drastically enhances hydrogen abstraction from methanol by OH at low temperature"' by D. Heard, R. Shannon, J. Gomez Martin, R. Caravan, M. Blitz, J. Plane, M. Antiñolo, M. Agundez, E. Jimenez, B. Ballesteros, A. Canosa, G. El Dib, J. Albaladejo and J. Cernicharo, Phys. Chem. Chem. Phys. 20 (2018) 8355–8357, https://doi.org/10.1039/C8CP00519B.
[47] I. Mosquera-Lois, D. Ferro-Costas, A. Fernández-Ramos, Chemical reactivity from the vibrational ground-state level. The role of the tunneling path in the tautomerization of urea and derivatives, Phys. Chem. Chem. Phys. 22 (2020) 24951–24963, https://doi.org/10.1039/D0CP04857G.
[48] D. Ferro-Costas, M.N.D.S. Cordeiro, A. Fernández-Ramos, An integrated protocol to study hydrogen abstraction reactions by atomic hydrogen in flexible molecules: application to butanol isomers, Phys. Chem. Chem. Phys. 24 (2022) 3043–3058, https://doi.org/10.1039/D1CP03928H.
[49] S. Kannath, P. Adamczyk, D. Ferro-Costas, A. Fernández-Ramos, D.T. Major, A. Dybala-Defratyka, Role of microsolvation and quantum effects in the accurate prediction of kinetic isotope effects: the case of hydrogen atom abstraction in ethanol by atomic hydrogen in aqueous solution, J. Chem. Theory Comput. 16 (2020) 847–859, https://doi.org/10.1021/acs.jctc.9b00774.
[50] D. Ferro-Costas, P.A. Sánchez-Murcia, A. Fernández-Ramos, Unraveling the catalytic mechanism of β-cyclodextrin in the vitamin D formation, J. Chem. Inf. Model. 64 (2024) 3865–3873, https://doi.org/10.1021/acs.jcim.3c02049.
[51] T.-H.T. Le, D. Ferro-Costas, A. Fernández-Ramos, M.A. Ortuño, Combined DFT and kinetic Monte Carlo study of UiO-66 catalysts for γ-valerolactone production, J. Phys. Chem. C 128 (2024) 1049–1057, https://doi.org/10.1021/acs.jpcc.3c06053.
[52] P. Chacon-Morales, A. Fernandez-Ramos, J. Gonzalez-Rodriguez, M.T. Moreira, E. Martinez-Nunez, D. Ferro-Costas, Computational data for the degradation of BPA under Fenton-type conditions, Zenodo (2025), https://doi.org/10.5281/zenodo.15654453 (accessed September 2025).
[53] A.J. Elliot, D.R. McCracken, Effect of temperature on $O^{\bullet-}$ reactions and equilibria: a pulse radiolysis study, Radiat. Phys. Chem. 33 (1989) 69–74, https://doi.org/10.1016/1359-0197(89)90096-9.
[54] L.K. Dhandole, Y.-S. Seo, S.-G. Kim, A. Kim, M. Cho, J.S. Jang, A mechanism study on the photocatalytic inactivation of *salmonella typhimurium* bacteria by Cu_xO loaded rhodium–antimony co-doped TiO_2 nanorods, Photochem. Photobiol. Sci. 18 (2019) 1092–1100, https://doi.org/10.1039/C8PP00460A.
[55] T. Liu, L. Wang, X. Lu, J. Fan, X. Cai, B. Gao, R. Miao, J. Wang, Y. Lv, Comparative study of the photocatalytic performance for the degradation of different dyes by $ZnIn_2S_4$: adsorption, active species, and pathways, RSC Adv. 7 (2017) 12292–12300, https://doi.org/10.1039/C7RA00199A.
[56] J. González-Rodríguez, L. Fernández, Z. Vargas-Osorio, C. Vázquez-Vázquez, Y. Piñeiro, J. Rivas, G. Feijoo, M.T. Moreira, Reusable Fe3O4/SBA15 nanocomposite as an efficient photo-Fenton catalyst for the removal of sulfamethoxazole and Orange II, Nanomaterials 11 (2021) 533, https://doi.org/10.3390/nano11020533.
[57] A. Fernández-Ramos, B.A. Ellingson, R. Meana-Pañeda, J.M.C. Marques, D. G. Truhlar, Symmetry numbers and chemical reaction rates, Theor. Chem. Accounts 118 (2007) 813–826, https://doi.org/10.1007/s00214-007-0328-0.
[58] K. Fukui, The path of chemical reactions - the IRC approach, Acc. Chem. Res. 14 (1981) 363–368, https://doi.org/10.1021/ar00072a001.
[59] M.J. Frisch, G.W. Trucks, H.B. Schlegel, G.E. Scuseria, M.A. Robb, J.R. Cheeseman, G. Scalmani, V. Barone, G.A. Petersson, H. Nakatsuji, X. Li, M. Caricato, A. V. Marenich, J. Bloino, B.G. Janesko, R. Gomperts, B. Mennucci, H.P. Hratchian, J. V. Ortiz, A.F. Izmaylov, J.L. Sonnenberg, F. Ding Williams, F. Lipparini, F. Egidi, J. Goings, B. Peng, A. Petrone, T. Henderson, D. Ranasinghe, V.G. Zakrzewski, J. Gao, N. Rega, G. Zheng, W. Liang, M. Hada, M. Ehara, K. Toyota, R. Fukuda, J. Hasegawa, M. Ishida, T. Nakajima, Y. Honda, O. Kitao, H. Nakai, T. Vreven, K. Throssell, J.A. Montgomery Jr., J.E. Peralta, F. Ogliaro, M.J. Bearpark, J. J. Heyd, E.N. Brothers, K.N. Kudin, V.N. Staroverov, T.A. Keith, R. Kobayashi,

J. Normand, K. Raghavachari, A.P. Rendell, J.C. Burant, S.S. Iyengar, J. Tomasi, M. Cossi, J.M. Millam, M. Klene, C. Adamo, R. Cammi, J.W. Ochterski, R.L. Martin, K. Morokuma, O. Farkas, J.B. Foresman, D.J. Fox, Gaussian 16 Rev. C.01, Wallingford, CT, 2016.

[60] V.K. Prasad, Z. Pei, S. Edelmann, A. Otero-de-la-Roza, G.A. DiLabio, BH9, a new comprehensive benchmark data set for barrier heights and reaction energies: assessment of density functional approximations and basis set incompleteness potentials, J. Chem. Theory Comput. 18 (2022) 151–166, https://doi.org/10.1021/acs.jctc.1c00694.

[61] A.V. Marenich, C.J. Cramer, D.G. Truhlar, Universal solvation model based on solute electron density and on a continuum model of the solvent defined by the bulk dielectric constant and atomic surface tensions, J. Phys. Chem. B 113 (2009) 6378–6396, https://doi.org/10.1021/jp810292n.

[62] E. Martínez-Núñez, An automated method to find transition states using chemical dynamics simulations, J. Comput. Chem. 36 (2015) 222–234, https://doi.org/10.1002/jcc.23790.

[63] E. Martínez-Núñez, An automated transition state search using classical trajectories initialized at multiple minima, Phys. Chem. Chem. Phys. 17 (2015) 14912–14921, https://doi.org/10.1039/C5CP02175H.

[64] E. Martinez-Nunez, G.L. Barnes, C. Bo, A. Fernández-Ramos, D. Ferro-Costas, D. Garay-Ruiz, D.R. Glowacki, S. Kopec, D. Pelaez-Ruiz, A. Rodriguez, R. Rodriguez-Fernandez, R.J. Shannon, J.J.P. Stewart, P.G. Tahoces, S.A. Vazquez, AutoMeKin, GitHub. https://github.com/emartineznunez/AutoMeKin (accessed September 2025).

[65] J.J.P. Stewart, MOPAC2016, Stewart Computational Chemistry, Colorado Springs, CO, USA, 2016.

[66] J. Baker, An algorithm for the location of transition states, J. Comput. Chem. 7 (1986) 385–395, https://doi.org/10.1002/jcc.540070402.

[67] D. Garay-Ruiz, amk_tools, GitHub, 2021 https://github.com/dgarayr/amk_tools (accessed September 2025).

[68] D. Garay-Ruiz, M. Álvarez-Moreno, C. Bo, E. Martínez-Núñez, New tools for taming complex reaction networks: the unimolecular decomposition of indole revisited, ACS Phys. Chem. Au 2 (2022) 225–236, https://doi.org/10.1021/acsphyschemau.1c00051.

[69] J.J.P. Stewart, Optimization of parameters for semiempirical methods V: modification of NDDO approximations and application to 70 elements, J. Mol. Model. 13 (2007) 1173–1213, https://doi.org/10.1007/s00894-007-0233-4.

[70] Y. Zhao, N. González-García, D.G. Truhlar, Benchmark database of barrier heights for heavy atom transfer, nucleophilic substitution, association, and unimolecular reactions and its use to test theoretical methods, J. Phys. Chem. A 109 (2005) 2012–2018, https://doi.org/10.1021/jp045141s.

[71] H. Eyring, The activated complex in chemical reactions, J. Chem. Phys. 3 (1935) 107–115, https://doi.org/10.1063/1.1749604.

[72] L.E. Rush, P.G. Pringle, J.N. Harvey, Computational kinetics of cobalt-catalyzed alkene hydroformylation, Angew. Chem. Int. Ed. 53 (2014) 8672–8676, https://doi.org/10.1002/anie.201402115.

[73] W.-P. Hu, D.G. Truhlar, Factors affecting competitive ion−molecule reactions: $ClO^- + C_2H_5Cl$ and C_2D_5Cl via E2 and S_N2 channels, J. Am. Chem. Soc. 118 (1996) 860–869, https://doi.org/10.1021/ja952464g.

[74] R. Xiao, L. Gao, Z. Wei, R. Spinney, S. Luo, D. Wang, D.D. Dionysiou, C.J. Tang, W. Yang, Mechanistic insight into degradation of endocrine disrupting chemical by hydroxyl radical: an experimental and theoretical approach, Environ. Pollut. 231 (2017) 1446–1452, https://doi.org/10.1016/j.envpol.2017.09.006.

[75] R.A. Torres, F. Abdelmalek, E. Combet, C. Pétrier, C. Pulgarin, A comparative study of ultrasonic cavitation and Fenton's reagent for bisphenol a degradation in deionised and natural waters, J. Hazard. Mater. 146 (2007) 546–551, https://doi.org/10.1016/j.jhazmat.2007.04.056.

[76] J. Poerschmann, U. Trommler, T. Górecki, Aromatic intermediate formation during oxidative degradation of bisphenol a by homogeneous sub-stoichiometric Fenton reaction, Chemosphere 79 (2010) 975–986, https://doi.org/10.1016/j.chemosphere.2010.03.030.

[77] Q. Huang, W.J. Weber, Transformation and removal of bisphenol a from aqueous phase via peroxidase-mediated oxidative coupling reactions: efficacy, products, and pathways, Environ. Sci. Technol. 39 (2005) 6029–6036, https://doi.org/10.1021/es050036x.

[78] H. Katsumata, S. Kawabe, S. Kaneco, T. Suzuki, K. Ohta, Degradation of bisphenol a in water by the photo-Fenton reaction, J Photochem Photobiol A Chem 162 (2004) 297–305, https://doi.org/10.1016/S1010-6030(03)00374-5.

[79] Z. Guo, R. Feng, Ultrasonic irradiation-induced degradation of low-concentration bisphenol a in aqueous solution, J. Hazard. Mater. 163 (2009) 855–860, https://doi.org/10.1016/j.jhazmat.2008.07.038.

[80] R.A. Torres, C. Pétrier, E. Combet, M. Carrier, C. Pulgarin, Ultrasonic cavitation applied to the treatment of bisphenol A. Effect of sonochemical parameters and analysis of BPA by-products, Ultrason. Sonochemistry 15 (2008) 605–611, https://doi.org/10.1016/j.ultsonch.2007.07.003.

[81] B. Gözmen, M.A. Oturan, N. Oturan, O. Erbatur, Indirect electrochemical treatment of bisphenol a in water via electrochemically generated Fenton's reagent, Environ. Sci. Technol. 37 (2003) 3716–3723, https://doi.org/10.1021/es034011e.

[82] Y. Wang, L. Wang, F. Ma, Y. You, FeOx@graphitic carbon core–shell embedded in microporous N-doped biochar activated peroxydisulfate for removal of bisphenol a: multiple active sites induced non-radical/radical mechanism, Chem. Eng. J. 438 (2022) 135552, https://doi.org/10.1016/j.cej.2022.135552.

[83] X. Zhao, P. Du, Z. Cai, T. Wang, J. Fu, W. Liu, Photocatalysis of bisphenol A by an easy-settling titania/titanate composite: effects of water chemistry factors, degradation pathway and theoretical calculation, Environ. Pollut. 232 (2018) 580–590, https://doi.org/10.1016/j.envpol.2017.09.094.

[84] L. Zhao, X. Xiao, L. Peng, F.L. Gu, R.Q. Zhang, Visible-light photocatalytic mechanism of bisphenol-A on nano-Bi_2O_3: a combined DFT calculation and experimental study, RSC Adv. 4 (2014) 10343–10349, https://doi.org/10.1039/C3RA46783J.

[85] A. Garg, T. Singhania, A. Singh, S. Sharma, S. Rani, A. Neogy, S.R. Yadav, V. K. Sangal, N. Garg, Photocatalytic degradation of bisphenol-A using N, co codoped TiO_2 catalyst under solar light, Sci. Rep. 9 (1) (2019) 765, https://doi.org/10.1038/s41598-018-38358-w.

[86] X. Xu, S. Zong, W. Chen, D. Liu, Comparative study of bisphenol A degradation via heterogeneously catalyzed H_2O_2 and persulfate: reactivity, products, stability and mechanism, Chem. Eng. J. 369 (2019) 470–479, https://doi.org/10.1016/j.cej.2019.03.099.

[87] T. Young, M. Geng, L. Lin, S.M. Thagard, Oxidative degradation of bisphenol A: a comparison between Fenton reagent, UV, UV/H_2O_2 and ultrasound, J. Adv. Oxid. Technol. 16 (2013) 89–101, https://doi.org/10.1515/jaots-2013-0109.

[88] F. Dai, X. Fan, G.R. Stratton, C.L. Bellona, T.M. Holsen, B.S. Crimmins, X. Xia, S. M. Thagard, Experimental and density functional theoretical study of the effects of Fenton's reaction on the degradation of bisphenol A in a high voltage plasma reactor, J. Hazard. Mater. 308 (2016) 419–429, https://doi.org/10.1016/j.jhazmat.2016.01.068.

[89] D. Zhou, F. Wu, N. Deng, W. Xiang, Photooxidation of bisphenol A (BPA) in water in the presence of ferric and carboxylate salts, Water Res. 38 (2004) 4107–4116, https://doi.org/10.1016/j.watres.2004.07.021.

[90] R. Frankowski, J. Płatkiewicz, E. Stanisz, T. Grześkowiak, A. Zgoła-Grześkowiak, Biodegradation and photo-Fenton degradation of bisphenol A, bisphenol S and fluconazole in water, Environ. Pollut. 289 (2021) 117947, https://doi.org/10.1016/j.envpol.2021.117947.

[91] J.C.C. da Silva, J.A. Reis Teodoro, R.J.d.C.F. Afonso, S.F. Aquino, R. Augusti, Photodegradation of bisphenol A in aqueous medium: monitoring and identification of by-products by liquid chromatography coupled to high-resolution mass spectrometry, Rapid Commun. Mass Spectrom. 28 (2014) 987–994, https://doi.org/10.1002/rcm.6863.